On the turbulence driving mode of expanding H II regions

Shyam H. Menon [●],[1][★] Christoph Federrath[1] and Rolf Kuiper[2]

[1]*Research School of Astronomy and Astrophysics, Australian National University, Canberra, ACT 2611, Australia*
[2]*Institute of Astronomy and Astrophysics, University of Tübingen, Auf der Morgenstelle 10, D-72076 Tübingen, Germany*

ABSTRACT

We investigate the turbulence driving mode of ionizing radiation from massive stars on the surrounding interstellar medium. We run hydrodynamical simulations of a turbulent cloud impinged by a plane-parallel ionization front. We find that the ionizing radiation forms pillars of neutral gas reminiscent of those seen in observations. We quantify the driving mode of the turbulence in the neutral gas by calculating the driving parameter b, which is characterized by the relation $\sigma_s^2 = \ln(1 + b^2 \mathcal{M}^2)$ between the variance of the logarithmic density contrast σ_s^2 [where $s = \ln(\rho/\rho_0)$ with the gas density ρ and its average ρ_0], and the turbulent Mach number $\mathcal{M}$. Previous works have shown that $b \sim 1/3$ indicates solenoidal (divergence-free) driving and $b \sim 1$ indicates compressive (curl-free) driving, with $b \sim 1$ producing up to ten times higher star formation rates than $b \sim 1/3$. The time variation of b in our study allows us to infer that ionizing radiation is inherently a compressive turbulence driving source, with a time-averaged $b \sim 0.76 \pm 0.08$. We also investigate the value of b of the pillars, where star formation is expected to occur, and find that the pillars are characterized by a natural mixture of both solenoidal and compressive turbulent modes ($b \sim 0.4$) when they form, and later evolve into a more compressive turbulent state with $b \sim 0.5$–0.6. A virial parameter analysis of the pillar regions supports this conclusion. This indicates that ionizing radiation from massive stars may be able to trigger star formation by producing predominately compressive turbulent gas in the pillars.

Key words: MHD – turbulence – H II regions.

1 INTRODUCTION

Stars predominantly form in dense, gravitationally bound gas inside giant molecular clouds (GMCs). Massive stars or clusters (OB associations) in these clouds produce UV radiation that dissociates and photoionizes the surrounding gas and results in the expansion of an ionization front (H II region). Photoionization increases the thermal pressure within GMCs, has the ability to mechanically unbind and destroy them (Williams & McKee 1997; Matzner 2002), and drives turbulence that may control the formation of the next generation of stars (Elmegreen & Scalo 2004; Mac Low & Klessen 2004; McKee & Ostriker 2007; Federrath & Klessen 2012; Padoan et al. 2014; Krumholz & Federrath 2019).

The expanding H II regions are also known to sculpt the surrounding neutral gas into structures reminiscent of the iconic 'Pillars of Creation' imaged by the *Hubble Space Telescope* (Hester et al. 1996). Since then, there have been a wealth of observations using multiwavelength surveys that image these pillars and related structures such as globules, energetic evaporating globules and

proplyds, and deduce dynamical quantities in and around them (Preibisch et al. 2012; Klaassen et al. 2014; Hartigan et al. 2015; Schneider et al. 2016; Klaassen et al. 2018; Klaassen et al. 2019). Models proposed to explain their formation lie broadly in two categories: the classic collect-and-collapse model by Elmegreen & Lada (1977) where the H II region sweeps up and accumulates cold gas creating density enhancements and eventually pillars in their shadows; or the more recent radiation-driven implosion (RDI) model where clouds with pre-existing density enhancements are sculpted to form pillars by impinging ionizing radiation. In these studies, the density enhancements are modelled as Bonnor–Ebert spheres or are seeded by turbulence, and they naturally produce the observed morphologies and dynamics of pillars (Mellema et al. 2006; Gritschneder et al. 2010; Mackey & Lim 2010; Walch et al. 2012; Tremblin et al. 2013).

Direct signatures of star formation are observed at the tip of these pillars through jets and outflows with suggestions that this star formation could be triggered by the ionizing radiation (Sugitani et al. 2002; Billot et al. 2010; Smith, Bally & Walborn 2010; Chauhan et al. 2011; Reiter & Smith 2013; Cortes-Rangel et al. 2019). However, the RDI picture of forming pillars raises the question as to whether star formation is really 'triggered', as

★ E-mail: shyam.menon@anu.edu.au

stars could have formed by the direct gravitational collapse of the pre-existing density enhancements anyway, and the ionizing radiation need not have enhanced local star formation in any way. In addition, numerical simulations have shown that photoionization may actually have a negative global net effect on star formation in GMCs, helping to explain the observed low star formation rates (Vázquez-Semadeni et al. 2010; Dale, Ercolano & Bonnell 2012; Colín, Vázquez-Semadeni & Gómez 2013; Gavagnin et al. 2017; Geen, Soler & Hennebelle 2017; Kim, Kim & Ostriker 2018). However, photoionization feedback may also simultaneously trigger star formation *locally*, by increasing the number of stars formed (but not necessarily the total mass of stars; Dale, Ercolano & Bonnell 2013). Moreover, Dale, Haworth & Bressert (2015) argues that current observational markers used to infer triggering may not be robust enough to distinguish whether an observed star was triggered or has spontaneously formed. Thus, there is no consensus on whether triggered star formation is effective on GMC scales, and hence resolving and understanding the local dynamics of the gas, in particular the turbulent flow is crucial for determining the role of photoionization for star formation.

Turbulence regulates star formation in molecular clouds and can play a dual role in the process: providing a form of support against self-gravitational collapse due to random velocity fluctuations, and on the other hand forming shocks resulting in overdensities that eventually undergo gravitational collapse (Mac Low & Klessen 2004). However, the observed supersonic turbulence (Elmegreen & Scalo 2004) must be driven by some external mechanism, as it would otherwise decay within one crossing time (Mac Low et al. 1998; Stone, Ostriker & Gammie 1998; Mac Low & Klessen 2004). Various agents for this driving have been proposed such as gravity, accretion, galactic rotation, shearing flows, stellar feedback, etc. (see Federrath et al. 2017; Federrath 2018, for a review of potential drivers), with the difference lying in the type of turbulent modes that they drive: compressive (curl-free) or solenoidal (divergence-free) modes. This difference is quantified through the driving parameter b, which typically varies between 1/3 and 1, where these two extreme cases refer to purely solenoidal and purely compressive driving, respectively (Federrath et al. 2010a). The value of b is important, as the flow dynamics, density structure, and the subsequent star formation rate depend on it (Federrath, Klessen & Schmidt 2008; Federrath et al. 2010a; Price, Federrath & Brunt 2011; Konstandin et al. 2012; Padoan et al. 2014; Federrath & Banerjee 2015; Nolan, Federrath & Sutherland 2015); with compressive driving resulting in broader density probability distribution functions (PDFs) and star formation rates approximately an order of magnitude larger than for solenoidal driving (Federrath & Klessen 2012; Federrath et al. 2016; Federrath 2018). The values of b have been studied systematically for different driving sources of turbulence in numerical simulations (Pan et al. 2016; Jin et al. 2017; Körtgen, Federrath & Banerjee 2017), and observations also find a significant variation in b across different clouds in the Milky Way (Padoan, Jones & Nordlund 1997; Brunt 2010; Ginsburg, Federrath & Darling 2013; Kainulainen, Federrath & Henning 2013; Federrath et al. 2016; Kainulainen & Federrath 2017).

Expanding H II regions have been proposed to be one of the primary sources of driving and maintaining supersonic turbulence in GMCs (Matzner 2002; Krumholz, Matzner & McKee 2006; Goldbaum et al. 2011). For instance, Gritschneder et al. (2009) simulate the ionizing irradiation of a local patch of a cloud ($\sim 4\,\mathrm{pc}$) and compare it to control runs without irradiation where the the initial turbulence is allowed to decay. They measure compressive, solenoidal, and total power spectra and find that turbulence is driven

significantly in the cold neutral gas, particularly in compressive modes, with more efficient driving on smaller scales, leading to a flatter power spectrum. However, there has been no systematic study of the driving parameter b based on density and velocity fluctuations for turbulence driven by expanding H II regions. Studying this would allow for more direct inferences on whether the local gas dynamics inside and around pillars shaped by the ionizing radiation support a picture of triggered star formation or not.

In this study, we calculate the driving parameter b of ionizing radiation-driven turbulence on the neutral gas in the vicinity of expanding H II regions. We perform numerical simulations analogous to Gritschneder et al. (2009), wherein we model the incoming radiation front as plane-parallel, and then calculate b from the previously established relation (Padoan et al. 1997; Federrath et al. 2008; Federrath et al. 2010a; Padoan & Nordlund 2011; Price et al. 2011; Konstandin et al. 2012; Molina et al. 2012; Hopkins 2013; Federrath & Banerjee 2015; Nolan et al. 2015; Squire & Hopkins 2017; Mandal, Federrath & Körtgen 2019):

$$\sigma_s^2 = \ln\left(1 + b^2 \mathcal{M}^2\right), \tag{1}$$

where σ_s is the standard deviation of the logarithmic density contrast $s = \ln(\rho/\rho_0)$ and the turbulent, sonic rms Mach number ($\mathcal{M}$). We further calculate the value of b for sub-parsec-scale regions at the tip of the formed pillar-like structures, where star formation is expected to occur.

In Section 2, we define the simulation set-up, initial condition, and the numerical methods we use in the simulations. In Section 3, we present our results and Section 4 provides a summary and conclusions.

2 NUMERICAL METHODS

2.1 Physics and numerical methods

To model the evolution of the cloud and ionizing radiation, we follow the equations of compressible 3D hydrodynamics in combination with an incoming plane-parallel photoionizing radiation flux in the x-direction of the Cartesian computational domain. For the hydrodynamics, we utilize the open source code PLUTO (Mignone et al. 2007, 2012) in version 4.1. For the photoionization feedback, we use the SEDNA module, a ray-tracing radiation transport solver, introduced in Kuiper & Hosokawa (2018). This solver combination was also used for a recent code benchmark (Bisbas et al. 2015). To generate the initial turbulent interstellar medium set-up, we implement the turbulence generator described in Federrath et al. (2008, 2010a).

2.2 Initial conditions

Our simulation set-up is largely similar to that of the fiducial simulation in Gritschneder et al. (2009). The initial set-up is a uniform Cartesian grid of length $L = 4\,\mathrm{pc}$ containing $1000\,\mathrm{M}_\odot$ of neutral gas at a temperature of $T_{\mathrm{neutral}} = 10\,\mathrm{K}$ corresponding to a sound speed of $c_s = 0.28\,\mathrm{km\,s^{-1}}$. To initialize a neutral turbulent state, we introduce supersonic velocity fluctuations with an rms Mach number of 10, i.e. $\mathcal{M} = \sigma_v/c_s = 10$, the ratio of turbulent velocity dispersion and sound speed, with a velocity power spectrum following $E(k) \propto k^{-2}$ (Federrath 2013; Federrath et al. 2010a), consistent with supersonic molecular cloud turbulence (Larson 1981; Solomon et al. 1987; Brunt & Heyer 2002; Ossenkopf & Mac Low 2002; Roman-Duval et al. 2011). These velocity fluctuations are introduced in the wavenumber range $2 \leq k/(2\pi/L) \leq 20$, with
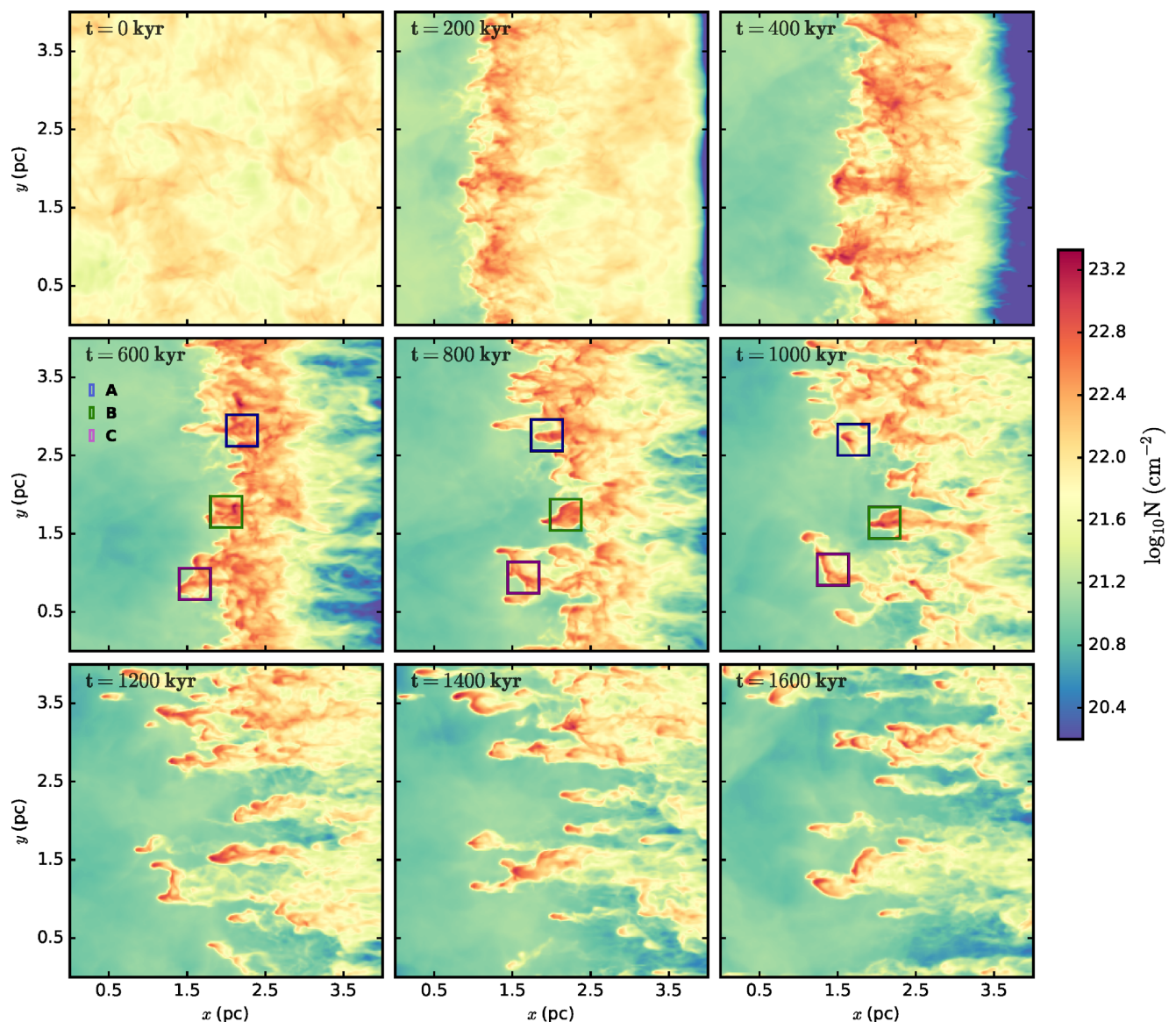
Figure 1. Time evolution of the column density of the gas integrated along the z-direction. The UV ionizing radiation enters the computational volume from the $x = 0$ face. The radiation ionizes parts of the cloud that sculpts pillar-like columns of neutral gas with the densest parts at its tips. The boxes in the second row of panels indicate three sub-parsec scale (~ 0.4 pc) regions containing the tips of pillars where we individually analyse the turbulence driving mode.

a natural mixture of solenoidal and compressive modes ($b \sim 0.4$; see fig. 8 in Federrath et al. 2010a). This is enforced by applying a projection in Fourier space, which decomposes the driving field into its solenoidal and compressive components (Federrath et al. 2008; 2010a). We then allow the turbulence to develop self-consistently by evolving the gas hydrodynamically with an isothermal equation of state for one turbulent crossing time given by $t_{\text{crossing}} = L/\sigma_v$, where σ_v is the velocity dispersion. The computational volume boundaries are periodic in all spatial directions during this phase. The turbulent state obtained after $t = t_{\text{crossing}}$ has a Mach number of ~ 3.5 due to the decay of the initial turbulence. We show a column density projection of this stage in Fig. 1 (top left-hand panel), which serves as the initial condition for the subsequent evolution of the cloud when it is hit by the ionization front entering from the left-hand side of the x-axis. We define this stage as time $t = 0$ from here on.

2.3 Simulation set-up

After this turbulent state is reached ($t = 0$), we introduce the ionizing radiation of a massive star on to the turbulent gas. As we are interested in a local region of a molecular cloud at the edge of the Strömgren sphere (Strömgren 1939), we approximate the ionization front as plane-parallel, impinging from the negative x-direction in the simulation domain. The photon flux per unit time is set to $F_{\text{Ly}} = 5 \times 10^9$ photons cm^{-2} s^{-1}. The ionization cross-section is set to 6.3×10^{-18} cm^2 and the recombination rate into any state but the hydrogen ground state is set to 2.6×10^{-13} cm^3 s^{-1}, using the so-called on-the-spot (OTS) approximation (Baker & Menzel 1938; Spitzer 1978; Osterbrock 1989). The ray tracer sets an ionization degree η at each cell from this flux, which is used to calculate the local temperature in the cell by linear interpolation:

$$T = T_{\text{ion}} \times \eta + T_{\text{neutral}} \times (1 - \eta), \qquad (2)$$

where $T_{\mathrm{neutral}} = 10\,\mathrm{K}$ and $T_{\mathrm{ion}} = 10^4\,\mathrm{K}$ are the neutral and ionized gas temperatures, respectively (Shu 1991). Both gas components can be approximated as being in thermal equilibrium since the heating and cooling time-scales are much shorter than the dynamical time-scale. The sound speeds $c_s = \sqrt{k_{\mathrm{B}} T/(\mu m_{\mathrm{H}})}$ associated with these phases are 0.28 and $12.84\,\mathrm{km\,s^{-1}}$, respectively, for atomic hydrogen gas with $\mu = 1.0$.

The fluid boundary conditions after switching on the radiation field are periodic in all directions except the x-direction, where semipermeable walls are imposed, i.e. we allow the gas to leave the computational domain through these boundaries, but do not allow new gas to enter. However, the expansion of the H II region expels the neutral gas in the cloud through the semipermeable boundary at $x = 4\,\mathrm{pc}$, compromising the study of turbulence driving as the gas leaves the computational domain too early. To delay this expulsion from the computational domain, we account for the bulk motion of the gas in the positive x-direction, by subtracting the instantaneous centre of mass velocity from each cell's local velocity at each integration step. This allows us to follow the evolution of the cloud and pillars in the rest frame of the system and for a sufficiently long time that includes the formation, evolution, and destruction (of some of) the pillars.

The adiabatic index (γ) of the ideal gas is set to 1.0001, which effectively establishes a locally isothermal state with the local temperature set by the ionization degree of the gas. For simplicity, we assume the gas is purely atomic with the mass per atom $m_{\mathrm{H}} = 1.6 \times 10^{-24}\,\mathrm{g}$. Note that we do not include magnetic fields, self-gravity, or a chemical network in our study. The grid resolution was set to 200^3 grid cells, and a single run took approximately 300 h on 140 compute cores. However, we also provide a resolution study to compare our main results for a grid resolution of 100^3, 200^3, and 400^3 grid cells, in Appendix A.

We note that the ray tracer solves the radiative transfer equation using the OTS approximation. This neglects the effect of the diffuse extreme ultraviolet (EUV) radiation emitted through recombinations in the surrounding ionized gas. This is believed to be responsible for shadows seen behind the pillars formed in other studies as well as our simulations and is an artefact of the uni-directional ray tracing performed in such a simulation set-up. This leads to parcels of low-density gas lying in the shadows of these pillars to remain neutral ($T \sim 10\,\mathrm{K}$), which would in reality be at much higher temperatures due to the EUV recombination field from the surrounding ionized gas. Numerical studies that include the diffuse radiation field find that shadow regions with low density are at least partly ionized and as a result the pillar structures are more compressed and less coherent (Ercolano & Gritschneder 2011; Haworth & Harries 2012). We account for this effect by excluding computational cells for which the temperature is inaccurate given their density, from the analysis, as explained in the results section next.

3 RESULTS

3.1 Gas structure and evolution

The initial turbulent state is shown in Fig. 1 (top left-hand panel). The ionization front is impinging on to this turbulent gas from the lower x-boundary of the computational domain (i.e. the $x = 0$ face). It instantly ionizes parts of gas in the cloud, with the radiation penetrating further into low-density channels, forming a shock front at the transition from ionized to neutral gas as can be seen at $t = 200\,\mathrm{kyr}$ in the second panel of Fig. 1. On further evolution, the

radiation continues to penetrate the low-density channels but fails to ionize columns of gas in the x-direction that contain overdensities seeded by the initial turbulent field. The ionized channels expand and through their thermal pressure push the neutral gas in their surroundings towards the columns of neutral gas in the shadows of overdensities. This process compresses the gas tangentially to the direction of the radiation and as a result, pillar-like structures form in the cold neutral gas (top-right-hand panel in Fig. 1). Further evolution unveils discernible pillar-like structures surrounded by a pool of hot ionized gas reminiscent to those seen in observations (three selected pillar regions are marked in the second row of Fig. 1). In addition to this thermal pressure-induced compression, the surrounding ionized gas can push off the neutral material, introducing a back reaction known as the 'rocket effect' that could exert significant forces and excite turbulent modes in the neutral gas (Krumholz, McKee & Bland-Hawthorn 2019). Note again that we are following the evolution in the rest frame of the entire system, which is why some of the pillars appear to move against the radiation direction.

Fig. 1 shows that the tips of the pillars have the highest density enhancements. It is at these pillar tips that star formation is observed to occur (e.g. Smith et al. 2010; Reiter & Smith 2013; Klaassen et al. 2014, 2019). Thus, we define three different pillar regions for a more detailed analysis next: pillars A, B, and C of sizes 0.4 pc in each direction. The regions are picked by eye from their line-integrated column densities in each direction while ensuring that the high-density tip of the pillar is included, and then adjusted such that the centre of mass of the region lies at the centre of the defined cubical box. These defined regions are shown for the line-integrated column density in the z-direction in Fig. 1 (second row and marked with boxes) for three different time snapshots during which we follow their evolution.

At later stages of the evolution ($t > 1000\,\mathrm{kyr}$), the ionizing radiation succeeds in photoevaporating or expelling a large fraction of neutral gas in the cloud. However, following the system in the instantaneous centre of mass frame of reference allows us to see the late time evolution of some pillars and isolated globules that manage to survive. Their survival can be attributed to the strong turbulent ram pressure in their interiors with comparable strengths to the thermal pressure of the ionized gas. Observations have revealed such structures in the vicinity of H II regions and they are usually categorized as globules, evaporating gaseous globules, condensations, and proplyds based on their morphology and sizes, and are proposed to eventually form from radiation sculpted pillar-like structures (see, for instance, Schneider et al. 2016).

3.2 Driving parameter b

The driving parameter b is a quantity that is proportional to the ratio of density to velocity fluctuations, $b \propto \sigma_\rho/\sigma_v$ in a supersonically turbulent cloud (Federrath et al. 2008; Federrath et al. 2010a). A velocity field that contains primarily compressible modes would produce stronger compressions and rarefactions and thus result in a higher spread in the density PDF than a primarily solenoidal velocity field. From the well-studied relation given by equation (1) between the log-density dispersion σ_s and the rms turbulent Mach number $\mathcal{M}$, we can rearrange for the driving parameter b:

$$b = \left\{ \left[\exp\left(\sigma_s^2\right) - 1 \right] / \mathcal{M}^2 \right\}^{1/2}. \tag{3}$$

Calculating b for an isothermal gas is fairly straightforward as the sound speed of isothermal gas is constant and identical everywhere, and $\mathcal{M}$ would just be the turbulent rms velocity dispersion (σ_v)

divided by that global sound speed. This condition is satisfied for time $t = 0\,\mathrm{kyr}$ in our simulation where all the gas is at $T \sim 10\,\mathrm{K}$, and we obtain a value of $b \sim 0.43$; which is the value expected for isothermal gas initialized with turbulent velocity fluctuations having a natural mixture of compressive and solenoidal modes (Federrath et al. 2010a).

However, for $t > 0$ the situation is more complicated as there are a range of local sound speeds due to the ionizing radiation, and thus a range of local Mach numbers (M). Thus, we have to distinguish the rms Mach number $\mathcal{M}$ from the local Mach number M. Strictly speaking, equation (3) is only valid for an isothermal gas, as it has been derived and tested under isothermal conditions, and we can thus only calculate b for the cold neutral gas in our simulations, i.e. by selecting regions of gas belonging to the cold neutral phase, and calculating the value of b for them.

3.2.1 Determining σ_s and $\mathcal{M}$ for the dense, cold gas

In this study, we are concerned with the turbulence in the star-forming neutral gas that is driven by the surrounding ionized gas when irradiated with ionizing radiation. Hence, we first pick out regions in our computational volume that have ionization fractions corresponding to neutral gas, i.e. $\eta < 10^{-7}$, which effectively corresponds to gas with temperature equal to the neutral gas temperature (i.e. $T = 10\,\mathrm{K}$).

In Fig. 2, we show a scatter plot for $t = 800\,\mathrm{kyr}$ of the local values of the scaled logarithmic density (s) and the Mach number (M), with the colour bar representing the mass-weighted probability density. We notice that over the wide range of s and *Mach* covered
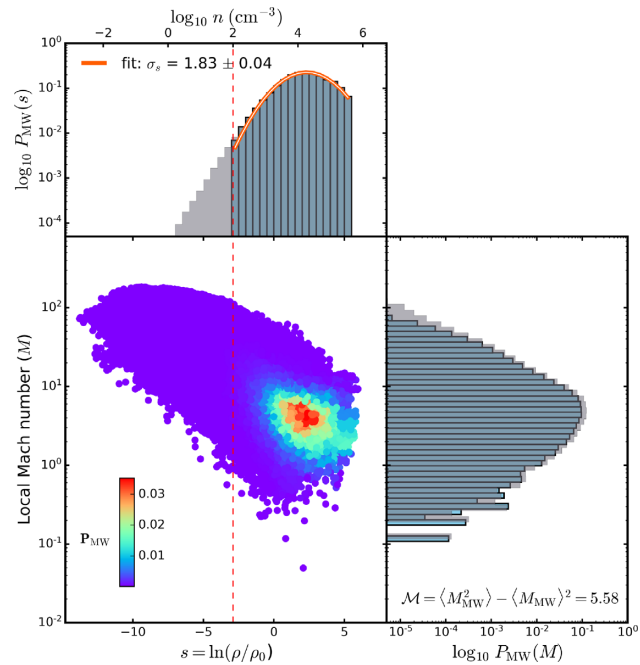

Figure 2. Scatter plot of local Mach numbers (M) and scaled logarithmic densities, $s = \ln(\rho/\rho_0)$, for the neutral gas in the entire simulation domain at time $t = 800\,\mathrm{kyr}$, colour coded by the mass-weighted probability density. The flanking histograms show the respective individual mass-weighted PDFs (grey) and the same for $n > 10^2\,\mathrm{cm}^{-3}$ (shaded blue). The derived value of σ_s from a lognormal fit (equation 4, shown in orange) and $\mathcal{M}$ from the mass-weighted standard deviation of M (computed from equation 5) are denoted in the respective panels. The values of σ_s and $\mathcal{M}$ obtained with this method are then used in equation (3) to compute the driving parameter b.

in the simulation, there is an anticorrelation between s and M, which is a result of the fact the gas is not globally isothermal (Federrath & Banerjee 2015). Moreover, the geometry of the pillar-like structures, with a high positive gradient in the density away from the ionized gas towards the confined dense columns, results in the lower density edges of the pillars having higher velocities compared to the denser interiors, leading to the anticorrelation. In contrast, equation (3) only holds for the dense, cold, near-isothermal gas, where s and M are un-correlated (Passot & Vázquez-Semadeni 1998; Kritsuk et al. 2007; Federrath et al. 2010a).

In addition to this, we notice that some of these low-density regions have extremely high local Mach numbers, with some of them exceeding $M \gtrsim 100$. Careful analysis of the data reveals that they lie at the shadows of the dense pillar tips, at the transition between the ionized and neutral phases of the gas, and the high velocities are the result of the large pressure gradient. However, as mentioned earlier, the cool temperatures of these regions ($T \sim 10\,\mathrm{K}$) are numerical artefacts due to the uni-directional ray-tracer used and the lack of a diffuse EUV recombination field and would in reality have higher ionization fractions (and hence higher c_s), which would effectively reduce their M to lower and more realistic values. To avoid the bias introduced by these artefacts, we (1) apply a density threshold of $n > n_{\mathrm{threshold}} = 10^2\,\mathrm{cm}^{-3}$ and (2) use mass-weighted PDFs, such that the low-density regions with unrealistic values of M do not contribute significantly to the density and velocity moments that enter equation (3). This method allows us to measure the turbulence driving parameter b for the dense, cold phase of neutral gas, where star formation would occur.

The flanking histograms in Fig. 2 show the mass-weighted PDFs for s (integrated over M) and M (integrated over s). The density threshold $n > n_{\mathrm{threshold}} = 10^2\,\mathrm{cm}^{-3}$ is indicated as a vertical dotted line, where $n_{\mathrm{threshold}}$ is the number density of the transition from atomic to molecular gas via surface reactions on dust grains. This value has been studied to lie in the range 100–$1000\,\mathrm{cm}^{-3}$ (Glover & Mac Low 2007; Glover et al. 2010). Here, we simply use $n_{\mathrm{threshold}} = 10^2\,\mathrm{cm}^{-3}$, however, we also repeat our analyses for $n_{\mathrm{threshold}} = 1000\,\mathrm{cm}^{-3}$ in Appendix B and show that our results do not change significantly with the chosen density threshold. The shaded flanking PDFs overlaid on the overall neutral gas PDFs in Fig. 2 show the distributions with the density threshold applied.

We now derive values for σ_s and $\mathcal{M}$ from the distributions of s and M, respectively. For the distribution of s, we fit the mass-weighted version of a lognormal given by Li, Klessen & Mac Low (2003),

$$P_{\mathrm{LN}}(s)\,\mathrm{d}s = \frac{C\exp(s)}{\sqrt{2\pi\sigma_{s,\mathrm{MW}}^2}}\exp\left[-\frac{s - s_0 + \sigma_{s,\mathrm{MW}}^2/2}{2\sigma_{s,\mathrm{MW}}^2}\right]\mathrm{d}s, \quad (4)$$

where s_0 is mean value of s, $\sigma_{s,\mathrm{MW}}$ is the mass-weighted standard deviation in s, and C is a normalization constant. We free all three parameters in this relation and compute their best-fitting values using a least-squares approach. We then set σ_s to be equal to the best-fitting value of $\sigma_{s,\mathrm{MW}}$. To derive $\mathcal{M}$, we explicitly calculate the mass-weighted standard deviation of the local Mach number distribution given by

$$\mathcal{M} = \sqrt{\langle M_{\mathrm{MW}}^2 \rangle - \langle M_{\mathrm{MW}} \rangle^2}, \quad (5)$$

where $\langle M_{\mathrm{MW}}^2 \rangle$ and $\langle M_{\mathrm{MW}} \rangle$ are the mean squared and arithmetic mean of the mass-weighted M, respectively. Fig. 2 demonstrates this method of analysis for the time snapshot $t = 800\,\mathrm{kyr}$, with the derived values of σ_s from the lognormal fit and $\mathcal{M}$ for the
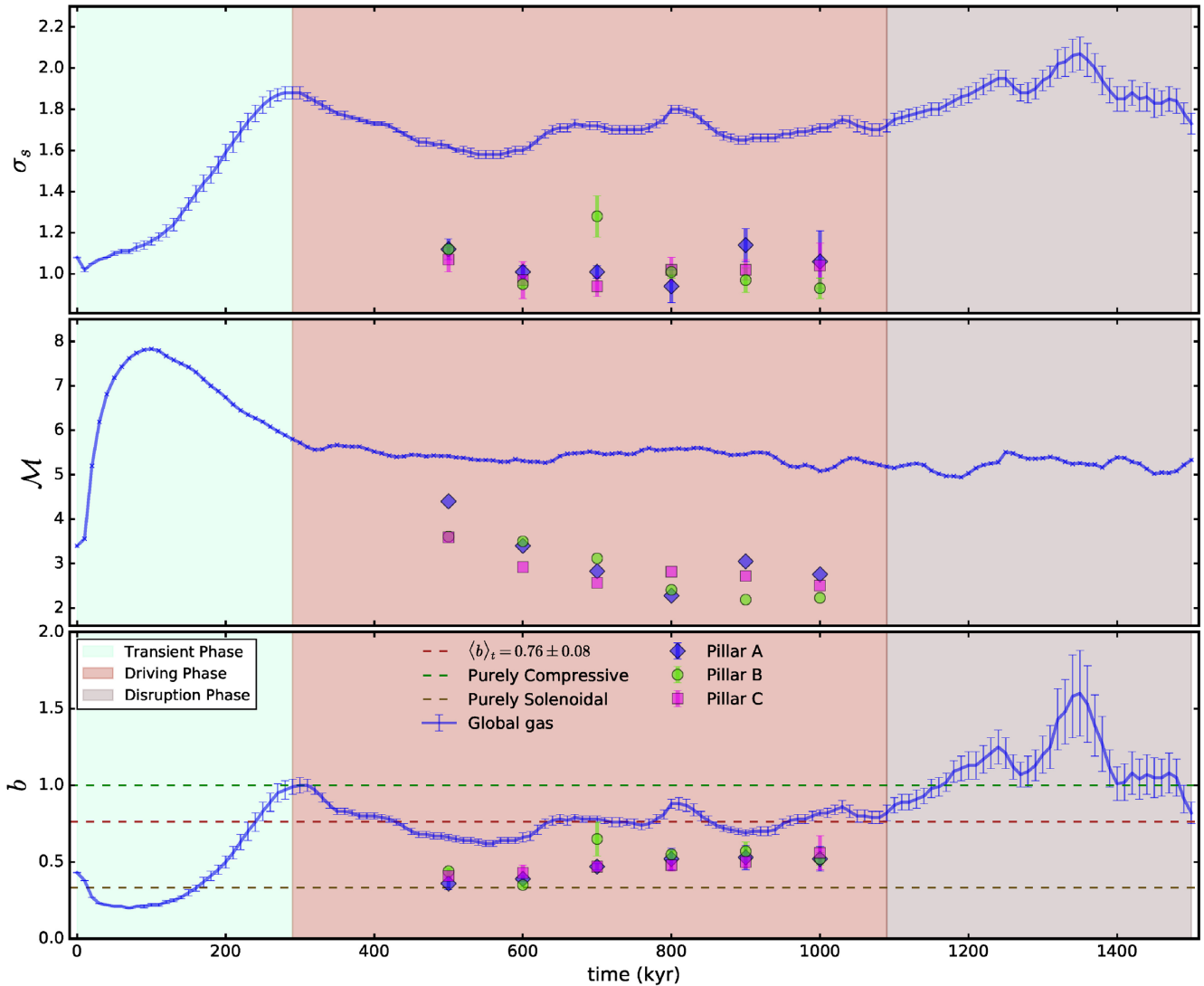
Figure 3. Evolution of the driving parameter b and the quantities involved in its calculation with time, where $t = 0$ is the time when the ionization front hits the gas. The shaded regions indicate the phase of evolution as categorized in Section 3.2.1. From top to bottom: logarithmic scaled density dispersion σ_s, rms Mach number $\mathcal{M}$, and driving parameter b. The dotted line in red indicates the time-averaged value of b in the driving phase $\langle b \rangle_t = 0.76 \pm 0.08$, and the values of b corresponding to purely compressive (green) and purely solenoidal (violet) modes are also provided for reference, as the dotted lines. The values of the same quantities obtained for the defined pillar regions (cf. Fig. 1), A (the diamonds), B (the circles), and C (the squares), are shown for five different time snapshots, where these could be reasonably defined and followed in their individual evolution.

dense, cold gas denoted on the flanking histograms. This method is repeated for each time snapshot to obtain the time evolution of b.

3.2.2 Time evolution of the global driving parameter b

Fig. 3 shows the time evolution of b with the method outlined in the previous sub-section. We divide this time evolution into three broad temporal phases:

(i) Transient phase ($0 \leq t < 300$ kyr): the gas ionized by the radiation field is in the process of enhancing the initial overdensities seeded by the turbulence and sculpting pillar-like regions. The turbulence driven by the thermal pressure-induced compression of neutral gas, as evident from a sharply increasing value of $\mathcal{M}$, pushes neutral gas from lower density columns into denser ones, resulting in an enhancement of the initial overdensities and increasing σ_s. We

observe a time lag in the increase of σ_s and $\mathcal{M}$, as one is the cause (higher $\mathcal{M}$) and the other the effect (higher σ_s), and this lag biases the value of b to be lower at very early times (up to ~ 200 kyr). When the velocity fluctuations start to succeed in enhancing the initial overdensities by dissipating their energy in shocks, $\mathcal{M}$ starts to decrease until it reaches a steady value of $\mathcal{M} \sim 5.5$.

(ii) Driving phase ($300 \leq t < 1100$ kyr): pillar-like structures have already been created as a result of the ionizing radiation-driven compression and the dynamics of the neutral gas have been established, albeit subject to local structural changes due to compression or photoevaporation at the individual pillar regions (as seen from the temporal fluctuations in σ_s). We thus call this phase the 'Driving Phase', as the turbulence has settled down and thus a driving parameter b can be reasonably defined here. As we can see in Fig. 3, a fairly stationary value of b is obtained in this phase. We calculate the time-averaged value of b in this phase as $\langle b \rangle_t = 0.76 \pm 0.08$.

(iii) Disruption phase ($1100 \leq t < 1500\,\mathrm{kyr}$): at these late times of the evolution, many of the neutral pillar-like structures get either expelled through the outflow boundaries of the computational box and/or get successfully ionized by the expanding H II region. The amount of neutral molecular gas available in the cloud is insufficient to derive meaningful statistics, as is evident from the relatively large error bars in this final phase of evolution.

We thus argue that the value of b obtained in what we call the 'driving phase' most sensibly represents what could be characterized as the turbulence driving mode of ionizing radiation. The time-averaged $b \sim 0.76$ suggests that the turbulence driven in the neutral molecular gas by the ionizing radiation on cloud scales ($\sim 4\,\mathrm{pc}$) is predominantly compressive ($b > 0.4$) in nature.

3.3 Pillar regions

Studies show that star formation is observed at the tips of pillar-like structures in a molecular cloud irradiated by ionizing radiation. Information on the local dynamics of the region is thus important to understand the star formation potential of the gas. Hence, we now calculate the driving parameter b separately for the three sub-parsec-scale pillar regions denoted in Fig. 1, namely pillars A, B, and C. The regions all have cubical sizes of $(0.4\,\mathrm{pc})^3$, adjusted such that the centre of mass of the region lies at the centre of the defined cubical box. We then select again only the neutral gas in these regions ($\eta < 10^{-7}$). However, we do not set any density threshold for pillar regions as the contribution of gas with $n < n_{\mathrm{threshold}}$ is negligible. We derive the Mach number ($\mathcal{M}$) as we did for the global gas, i.e. as the standard deviation of the mass-weighted distribution of the local Mach number (M), and given by equation (5). However, the distribution of s is more skewed, and a symmetrical lognormal does not fit the data well on the local pillar scales, most likely because of intermittency in the turbulence (Kritsuk et al. 2007; Federrath et al. 2010a; Hopkins 2013; Squire & Hopkins 2017). To account for this skewness, we instead fit the mass-weighted version of the Hopkins (2013) intermittency PDF model,

$$p_{\mathrm{HK}}(s)\,\mathrm{d}s = Ce^s I_1(2\sqrt{\lambda\omega(s)})\exp\left[-(\lambda+\omega(s))\right]\sqrt{\frac{\lambda}{\theta^2\omega(s)}}\,\mathrm{d}s,$$

$$\lambda = \frac{\sigma_{s,\mathrm{MW}}^2(1+\theta)^3}{2\theta^2}, \quad \omega(s) = \lambda/(1+\theta) - s/\theta \; (\omega \geq 0),$$

(6)

where $I_1(x)$ is the first-order modified Bessel function of the first kind, $\sigma_{s,\mathrm{MW}}$ is the mass-weighted standard deviation in s, and θ is the intermittency parameter. Note that in the zero-intermittency limit ($\theta \to 0$) equation (6) simplifies to the lognormal PDF. We fit equation (6) to $P_{\mathrm{MW}}(s)$ and determine the best-fitting $\sigma_{s,\mathrm{MW}}$. We show the scatter of s and M, their corresponding mass-weighted histograms, and the values of σ_s and $\mathcal{M}$ in Fig. 4 for time snapshot $t = 800\,\mathrm{kyr}$. These are then used in equation (3) to obtain the value of b. This is repeated for five different time snapshots in the driving phase and the obtained values were added in Fig. 3.

Fig. 3 shows that the values for σ_s and $\mathcal{M}$ for the pillar regions are lower than that for the gas on the global cloud scales. This is expected from the observed cloud scaling relations, such as the velocity dispersion–size relation. The pillar regions are considerably smaller ($\sim 0.4\,\mathrm{pc}$) and thus have only mildly supersonic velocity dispersions ($\mathcal{M} \sim 2$–4). The obtained velocity dispersions ($\mathcal{M} \times c_s$) are in the range 0.4–1 km s^{-1}, in agreement with observations of pillars on these scales (Klaassen et al. 2019).
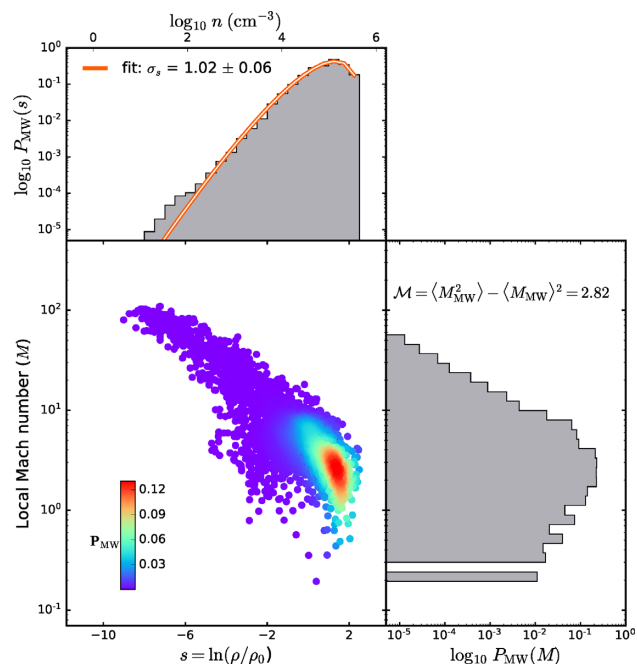

Figure 4. Same as Fig. 2, but for the sub-parsec region Pillar C at $t = 800\,\mathrm{kyr}$, demonstrating our analysis method to derive values of b for the three pillar regions. We do not use a density cut-off here as the contributions from $n < 100\,\mathrm{cm}^{-3}$ are negligible. We use the Hopkins (2013) intermittency PDF model (equation 6) instead of a standard lognormal to fit for σ_s (shown in orange).
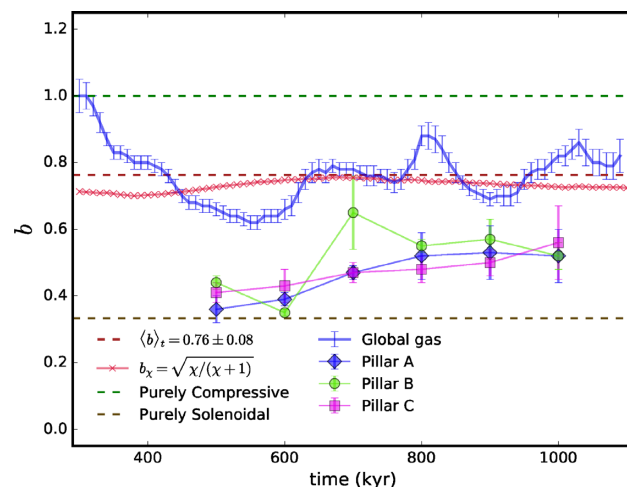

Figure 5. Zoom-in of the time evolution of the driving parameter b during the driving phase for the three pillar regions. The dotted lines indicate purely compressive (green) and purely solenoidal (brown) values of b for reference. The solid lines indicate the time evolution of b for the gas on $\sim 4\,\mathrm{pc}$ global cloud scales (blue) and the value of b inferred from the compressive ratio b_χ (red) discussed in Section 3.4.

The b values of the pillar regions are also somewhat smaller with $b \sim 0.4$–0.6 compared to the cloud-scale average. Interestingly, we find a noticeable time variation for each pillar region, individually. This is more clearly seen in Fig. 5, where we find that the value of b increases for each pillar, from a value of $b \sim 0.4$–0.55 as time progresses, indicating that the turbulence in these regions develops more compressive modes as they evolve. This might suggest that

conditions for star formation are progressively boosted in these regions, as the H II region moves through the cloud. That being said, commenting further on the potential star formation in these simulations is outside the scope of this work as it would require follow-up simulations that include self-gravity and a model for star formation such as the sink-particle technique (e.g. Federrath et al. 2010b).

3.4 The compressive ratio

So far we have primarily used the density dispersion and rms Mach number to study the turbulence driving parameter b of clouds hit by an ionization front. However, we can also look at the compressible-to-solenoidal mode mixture in the velocity field to obtain related information about b, via the so-called 'compressive ratio' (Kritsuk et al. 2007; Federrath et al. 2010a; Federrath et al. 2011; Pan et al. 2016; Körtgen et al. 2017). The compressive ratio is given by

$$\chi = \langle v_c^2 \rangle / \langle v_s^2 \rangle, \tag{7}$$

where v_c and v_s are the compressive and solenoidal components of the velocity field, respectively. In order to compute these two components, the velocity field is first corrected for bulk motion, such that only the turbulent fluctuations remain (analogous to χ_{turb} defined in Pan et al. 2016), and then density-weighted to trace the velocity field of the cold, dense gas. Both v_c and v_s are then derived through a Helmholtz decomposition of the turbulent velocity field in Fourier space. Following the suggestion of Pan et al. (2016), an effective driving parameter can be derived from this value of χ given by $b_\chi = \sqrt{\chi/(\chi + 1)}$.

The evolution of b_χ during the Driving Phase is shown in Fig. 5. As we can see, the value we obtain remains more or less constant (~ 0.75) and indicates strong compressive velocity fields. This value is also very close to the time-averaged value $\langle b \rangle_t$ obtained earlier from the relation between the density and velocity fluctuations (equation 3). The fact that b obtained from the σ_s–$\mathcal{M}$ relation (equation 1) agrees with that obtained from the modes in the velocity field (b_χ) is encouraging and supports our overall conclusions of a relatively compressive turbulence driving parameter ($b > 0.4$) for clouds compressed in H II regions.

3.5 Virial parameter

The virial parameter is a dimensionless quantity that characterizes the ratio of turbulent kinetic energy to gravitational energy of a cloud of gas (Bertoldi & McKee 1992), with its general form given by (Federrath & Klessen 2012)

$$\alpha_{\mathrm{vir}} = 2E_{\mathrm{kin}}/|E_{\mathrm{grav}}|, \tag{8}$$

where E_{kin} and E_{grav} are the kinetic and potential energies of the cloud, respectively. A value of $\alpha_{\mathrm{vir}} < 1$ suggests that the cloud could be gravitationally unstable and thus potentially form stars, with the star formation rate per free-fall time SFR$_{\mathrm{ff}}$ increasing with decreasing α_{vir} (Krumholz & McKee 2005; Hennebelle & Chabrier 2011; Federrath & Klessen 2012; Padoan, Haugbølle & Nordlund 2012).

We therefore study the time evolution of α_{vir} for our defined pillar regions to test whether the driving of compressive turbulence is accompanied by an increase in the star formation capability of the gas. We calculate α_{vir} by computing the self-gravitational potential Φ for each pillar region from their respective density distributions, with boundary conditions taking into account the density distribution of gas outside the boundaries of the pillar
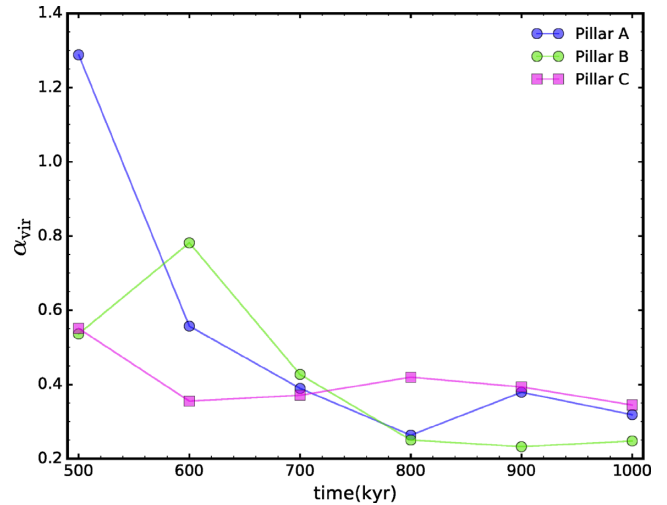

Figure 6. Time evolution of the virial parameter α_{vir} computed with equation (9) for each of the three pillar regions.

regions. This is important because the binding energy of pillars is not independent of the environment (Federrath & Klessen 2012), as these regions are not isolated, but instead are typically deeply embedded inside a larger molecular cloud complex. We calculate α_{vir} as

$$\alpha_{\mathrm{vir}} = \frac{\sum_{i \in \mathrm{P}} m_i |(\boldsymbol{v}_{\mathrm{turb}})_i|^2}{\sum_{i \in \mathrm{P}} m_i |\boldsymbol{\Phi}_i|}, \tag{9}$$

where P is the set of computational cells lying in the pillar region, m_i the mass, and $(\boldsymbol{v}_{\mathrm{turb}})_i$ the turbulent velocity in cell i. The time evolution of this calculated α_{vir} for the pillars is shown in Fig. 6.

As we can see, the value of α_{vir} goes down with time for all the pillar regions in our simulations. This is because the turbulent kinetic energy in the pillars is dissipated in shocks produced by the compressive turbulence (decreasing $|(\boldsymbol{v}_{\mathrm{turb}})_i|$ locally). This leads to the formation of local overdensities in the pillars (increasing $|\boldsymbol{\Phi}_i|$ locally), which effectively results in lower values of α_{vir}. This suggests that the driving of compressive turbulence in the pillars lowers the value of the virial parameter and as a result, could potentially trigger star formation in them. We note that there are alternatives to equation (9) to calculate the virial parameter, especially in observational studies where the self-gravitational potential is not available. In Appendix C, we test these different methods, and find that although there is a significant difference in the absolute values of α_{vir} obtained with different methods, the trend of a decreasing α_{vir} with time is independent of the choice of method.

4 SUMMARY AND CONCLUSIONS

In this study, we simulate the formation of pillar-like structures in turbulent clouds at the edge of a Strömgren sphere, by an expanding H II region modelled as an impinging plane-parallel ionizing front. We form structures that resemble observed pillars in morphology and dynamics, and study their evolution for up to 2 Myr. We infer the effective mode of turbulence that is driven by the ionization front in the dense, cold gas of the cloud, by calculating the turbulence driving parameter (b) in equation (1). We do the same for three different sub-parsec scale regions at the tip of pillars containing the densest gas, where star formation is often observed. Our main results can be summarized as follows:

(i) The value of b for the cold, dense gas in the cloud does not vary significantly with time during the driving phase (300–1100 kyr), with a time-averaged value of $\langle b \rangle_t = 0.76 \pm 0.08$. This suggests that expanding H II regions drive predominately compressive modes of turbulence.

(ii) The values of b calculated for the pillar regions are also primarily compressive albeit with lower values of $b \sim 0.4$–0.6 compared to the gas on global cloud scales. We also obtain values for the 3D velocity dispersion ($\sigma_v \sim 0.4$–$1\,\mathrm{km\,s^{-1}}$) that agree with observations in the pillar regions.

(iii) The turbulent modes for each of the pillar regions transition from a natural mixture of solenoidal and compressive modes ($b \sim 0.4$) to a compression-dominated regime ($b \sim 0.55$) during their lifetime, as the ionized gas continues to sculpt the pillars.

(iv) We calculate the compressive ratio (χ) for the cloud and infer a driving parameter $b_\chi \sim 0.75$ from it, consistent with the time-averaged global b value obtained from the density dispersion–Mach number relation, supporting our main conclusion that expanding H II regions drive primarily compressive modes of turbulence.

(v) The virial parameter α_{vir} decreases with time for the pillar regions, which suggests that the driving of compressive turbulence in these regions, as the H II region passes through the cloud, is accompanied by an increase in the star formation capability of the gas.

Our main finding of predominantly compressive turbulence driven in H II regions may be interpreted as promoting star formation, and hence leading to 'triggered star formation'. However, the converse effect of the neutral gas being photoevaporated by the radiation limits the extent of this triggering, and the net star formation occurring in the region is likely the result of the competition between these two processes. Follow-up simulations with self-gravity and sink particles to follow star formation would allow us to make more quantitative predictions on the net effect of photoionization on star formation in molecular clouds.

REFERENCES

Baker J. G., Menzel D. H., 1938, ApJ, 88, 52
Bertoldi F., McKee C. F., 1992, ApJ, 395, 140
Billot N., Noriega-Crespo A., Carey S., Guieu S., Shenoy S., Paladini R., Latter W., 2010, ApJ, 712, 797
Bisbas T. G. et al., 2015, MNRAS, 453, 1324
Brunt C. M., 2010, A&A, 513, A67
Brunt C. M., Heyer M. H., 2002, ApJ, 566, 289
Chauhan N., Pandey A. K., Ogura K., Jose J., Ojha D. K., Samal M. R., Mito H., 2011, MNRAS, 415, 1202
Colín P., Vázquez-Semadeni E., Gómez G. C., 2013, MNRAS, 435, 1701
Cortes-Rangel G., Zapata L. A., Toala J. A., Ho P. T. P., Takahashi S., Mesa-Delgado A., Masque J. M., 2019, AJ, 159, 62,
Dale J. E., Ercolano B., Bonnell I. A., 2012, MNRAS, 424, 377
Dale J. E., Ercolano B., Bonnell I. A., 2013, MNRAS, 431, 1062
Dale J. E., Haworth T. J., Bressert E., 2015, MNRAS, 450, 1199
Elmegreen B. G., Lada C. J., 1977, ApJ, 214, 725
Elmegreen B. G., Scalo J., 2004, Annual Review of Astronomy and Astrophysics, 42, 211
Ercolano B., Gritschneder M., 2011, MNRAS, 413, 401
Federrath C., 2013, MNRAS, 436, 1245
Federrath C., 2018, Phys. Today, 71, 38
Federrath C., Banerjee S., 2015, MNRAS, 448, 3297
Federrath C., Klessen R. S., 2012, ApJ, 761, 156
Federrath C., Klessen R. S., Schmidt W., 2008, ApJ, 688, L79
Federrath C., Roman-Duval J., Klessen R. S., Schmidt W., Mac Low M.-M., 2010a, A&A, 512, A81
Federrath C., Banerjee R., Clark P. C., Klessen R. S., 2010b, ApJ, 713, 269
Federrath C., Chabrier G., Schober J., Banerjee R., Klessen R. S., Schleicher D. R. G., 2011, Phys. Rev. Lett., 107, 114504
Federrath C. et al., 2016, ApJ, 832, 143
Federrath C. et al., 2017, Proceedings of the International Astronomical Union, 11(S322). p. 123
Gavagnin E., Bleuler A., Rosdahl J., Teyssier R., 2017, MNRAS, 472, 4155
Geen S., Soler J. D., Hennebelle P., 2017, MNRAS, 471, 4844
Ginsburg A., Federrath C., Darling J., 2013, ApJ, 779, 50
Glover S. C. O., Mac Low M.-M., 2007, ApJ, 659, 1317
Glover S. C. O., Federrath C., Mac Low M. M., Klessen R. S., 2010, MNRAS, 404, 2
Goldbaum N. J., Krumholz M. R., Matzner C. D., McKee C. F., 2011, ApJ, 738
Gritschneder M., Naab T., Walch S., Burkert A., Heitsch F., 2009, ApJ, 694
Gritschneder M., Burkert A., Naab T., Walch S., 2010, ApJ, 723, 971
Hartigan P., Reiter M., Smith N., Bally J., 2015, AJ, 149
Haworth T. J., Harries T. J., 2012, MNRAS, 420, 562
Hennebelle P., Chabrier G., 2011, ApJ, 743, L29
Hester J. J. et al., 1996, AJ, 111, 2349
Hopkins P. F., 2013, MNRAS, 430, 1880
Jin K., Salim D. M., Federrath C., Tasker E. J., Habe A., Kainulainen J. T., 2017, MNRAS, 469, 383
Kainulainen J., Federrath C., 2017, A&A, 608, L3
Kainulainen J., Federrath C., Henning T., 2013, A&A, 553, L8
Kim J.-G., Kim W.-T., Ostriker E. C., 2018, ApJ, 859, 68
Kitsionas S. et al., 2009, A&A, 508, 541
Klaassen P. D., Mottram J. C., Dale J. E., Juhasz A., 2014, MNRAS, 441, 656
Klaassen P. D. et al., 2018, A&A, 611, A99
Klaassen P. D., Reiter M. R., McLeod A. F., Mottram J. C., Dale J. E., Gritschneder M., 2019, MNRAS, 491, 178
Konstandin L., Girichidis P., Federrath C., Klessen R. S., 2012, ApJ, 761, 149
Körtgen B., Federrath C., Banerjee R., 2017, MNRAS, 472, 2496
Kritsuk A. G., Norman M. L., Padoan P., Wagner R., 2007, ApJ, 665, 416
Krumholz M. R., Federrath C., 2019, Frontiers Astron. Space Sci., 6, 7
Krumholz M. R., McKee C. F., 2005, ApJ, 630, 250
Krumholz M. R., Matzner C. D., McKee C. F., 2006, ApJ, 653, 361
Krumholz M. R., McKee C. F., Bland-Hawthorn J., 2019, ARA&A, 57, 227
Kuiper R., Hosokawa T., 2018, A&A, 616, A101
Larson R. B., 1981, MNRAS, 194, 809
Li Y., Klessen R. S., Mac Low M.-M., 2003, ApJ, 592, 975

Mac Low M.-M., Klessen R. S., Burkert A., Smith M. D., 1998, Phys. Rev. Lett., 80, 2754

Mackey J., Lim A. J., 2010, MNRAS, 403, 714

Mac Low M.-M., Klessen R. S., 2004, Rev. Mod. Phys., 76, 125

Mandal A., Federrath C., Körtgen B., 2020, MNRAS, 493, 3098

Matzner C. D., 2002, ApJ, 566, 302

McKee C. F., Ostriker E. C., 2007, Annual Review of Astronomy and Astrophysics, 45, 565

Mellema G., Arthur S. J., Henney W. J., Iliev I. T., Shapiro P. R., 2006, ApJ, 647, 397

Mignone A., Bodo G., Massaglia S., Matsakos T., Tesileanu O., Zanni C., Ferrari A., 2007, ApJS, 170, 228

Mignone A., Flock M., Stute M., Kolb S. M., Muscianisi G., 2012, A&A, 545, A152

Molina F. Z., Glover S. C. O., Federrath C., Klessen R. S., 2012, MNRAS, 423, 2680

Nolan C. A., Federrath C., Sutherland R. S., 2015, MNRAS, 451, 1380

Ossenkopf V., Mac Low M.-M., 2002, A&A, 390, 307

Osterbrock D. E., 1989, Astrophysics of Gaseous Nebulae and Active Galactic Nuclei. University Science Books, Mill Valley, CA

Padoan P., Jones B. J. T., Nordlund A. P., 1997, ApJ, 474, 730

Padoan P., Nordlund Å., 2011, ApJ, 730, 40

Padoan P., Haugbølle T., Nordlund Å., 2012, ApJ, 759, L27

Padoan P., Federrath C., Chabrier G., Evans N. J., II, Johnstone D., Jørgensen J. K., McKee C. F., Nordlund Å., 2014, in Beuther H., Klessen R. S., Dullemond C. P., Henning T., eds, Protostars and Planets VI. University of Arizona Press, Tucson, AZ, p. 77

Pan L., Padoan P., Haugbølle T., Nordlund Å., 2016, ApJ, 825, 30

Passot T., Vázquez-Semadeni E., 1998, Phys. Rev. E, 58, 4501

Preibisch T., Roccatagliata V., Gaczkowski B., Ratzka T., 2012, A&A, 541, A132

Price D. J., Federrath C., Brunt C. M., 2011, ApJ, 727, L21

Reiter M., Smith N., 2013, MNRAS, 433, 2226

Roman-Duval J., Federrath C., Brunt C., Heyer M., Jackson J., Klessen R. S., 2011, ApJ, 740, 120

Schneider N. et al., 2016, A&A, 591, A40

Shu F. H., 1991, Physics of Astrophysics, Vol. I. University Science Books, Mill Valley, CA

Smith N., Bally J., Walborn N. R., 2010, MNRAS, 405, 1153

Solomon P. M., Rivolo A. R., Barrett J., Yahil A., 1987, ApJ, 319, 730

Spitzer L., 1978, Physical Processes in the Interstellar Medium. John Wiley & Sons, Ltd, New York

Squire J., Hopkins P. F., 2017, MNRAS, 471, 3753

Stone J. M., Ostriker E. C., Gammie C. F., 1998, ApJ, 508, L99

Strömgren B., 1939, ApJ, 89, 526

Sugitani K. et al., 2002, ApJ, 565, L25

Tremblin P. et al., 2013, A&A, 560, A19

Vázquez-Semadeni E., Colín P., Gómez G. C., Ballesteros-Paredes J., Watson A. W., 2010, ApJ, 715, 1302

Walch S. K., Whitworth A. P., Bisbas T., Wünsch R., Hubber D., 2012, MNRAS, 427, 625

Williams J. P., McKee C. F., 1997, ApJ, 476, 166

APPENDIX A: RESOLUTION STUDY

The decay rate of the turbulent energy and the general properties of turbulence in numerical simulations depend on the numerical resolution adopted, with lower resolution showing, e.g. a larger (artificial) decay (Mac Low et al. 1998; Federrath 2013). In order to test numerical convergence of our results, we compare σ_s, $\mathcal{M}$, and the resulting b parameter (from equation 3) for three different numerical grid resolutions: 100^3 ($\Delta x = 0.04$ pc), 200^3 ($\Delta x = 0.02$ pc), and 400^3 ($\Delta x = 0.01$ pc). We note that the 400^3 simulation has only been followed for comparison purposes up to ~ 800 kyr due to the computational cost of that simulation. Fig. A1 shows the scatter plot and corresponding PDFs of s and M for the three different resolutions at $t = 700$ kyr, and Fig. A2 compares the time evolution of σ_s, $\mathcal{M}$, and b derived from the PDFs, following the method explained in the main part of the manuscript. We can see that $\mathcal{M}$ is almost independent of the choice of resolution (as long as the grid resolution is at least 100^3). However, σ_s and b show a systematic increase between 100^3 and 200^3, while for $\gtrsim 200^3$, the resulting σ_s and b are close to the values obtained for 200^3 grid cells. Similar trends for the dependence of $\mathcal{M}$ and σ_s are seen in Federrath et al. (2010a), Kitsionas et al. (2009), and later resolution studies. We thus conclude that a spatial resolution of $\lesssim 0.02$ pc is sufficient to achieve reasonable convergence in this type of simulation.
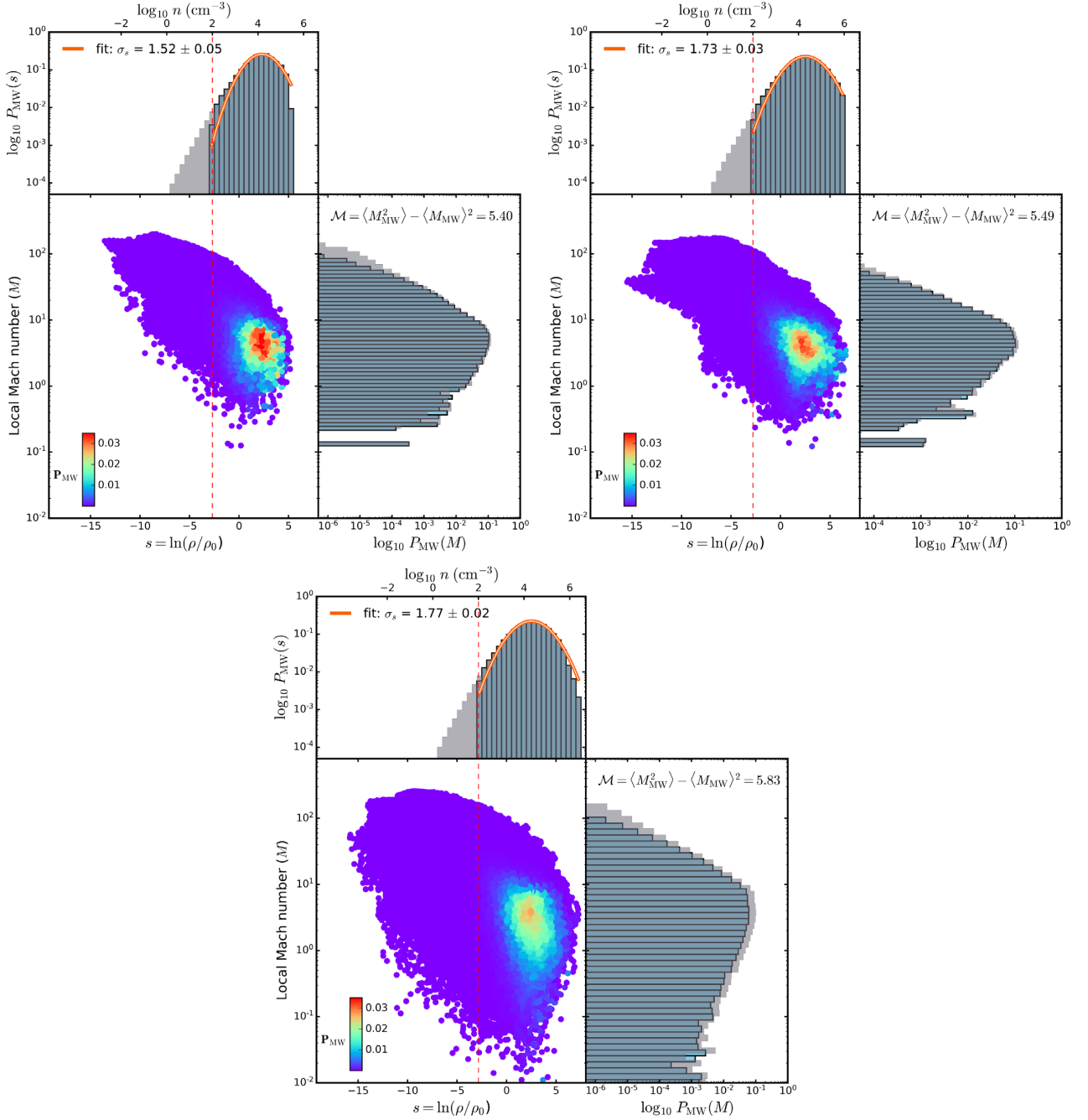
Figure A1. Scatter plot and flanking histograms (similar to Fig. 2) for $t = 700\,\mathrm{kyr}$ comparing three different numerical grid resolutions. Top left : 100^3 ($\Delta x = 0.04\,\mathrm{pc}$), top right : 200^3 ($\Delta x = 0.02\,\mathrm{pc}$), and bottom: 400^3 ($\Delta x = 0.01\,\mathrm{pc}$).
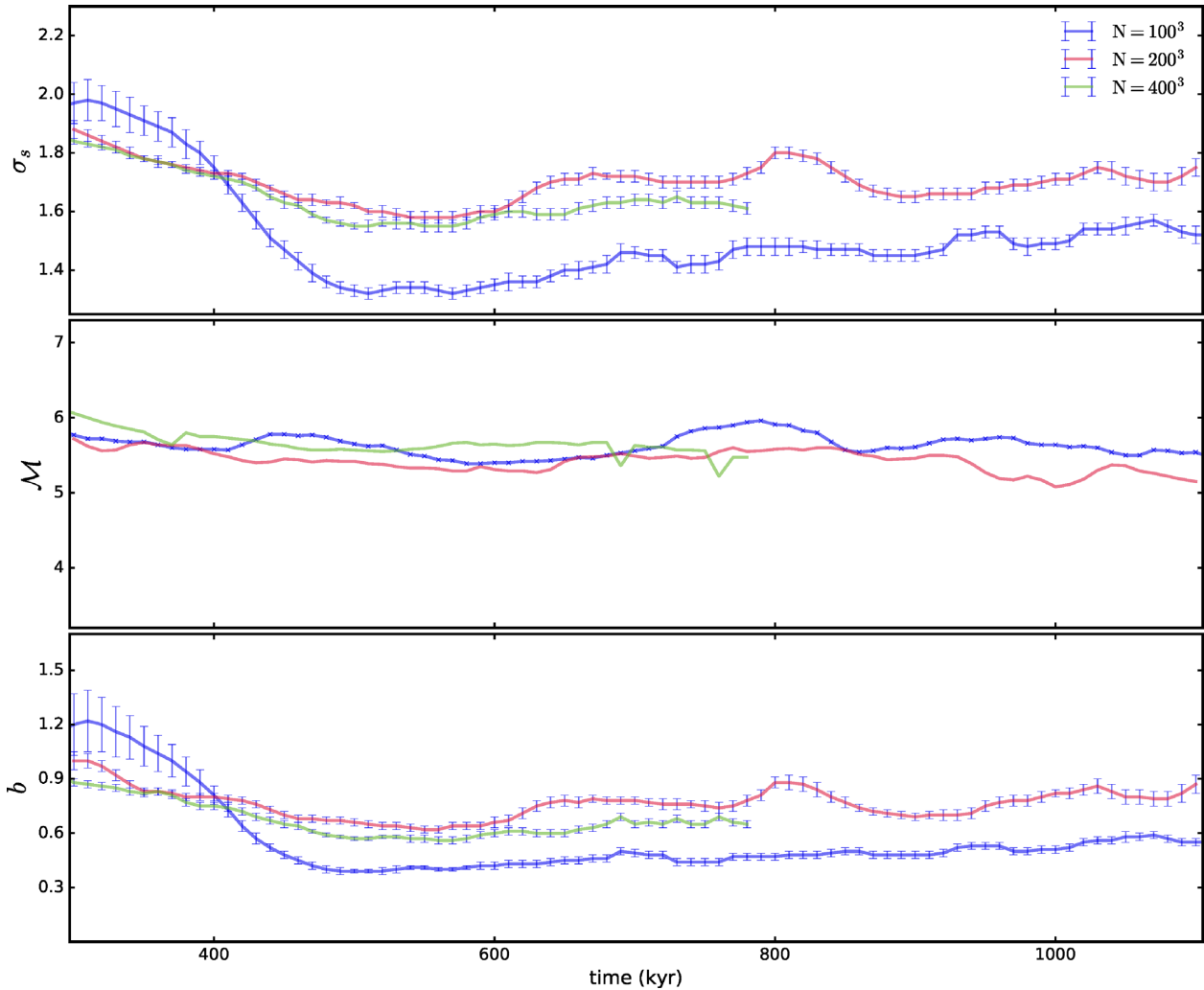
Figure A2. The values of σ_s, $\mathcal{M}$, and b compared for simulations with resolutions of 100^3 ($\Delta x = 0.04\,\mathrm{pc}$), 200^3 ($\Delta x = 0.02\,\mathrm{pc}$) and 400^3 ($\Delta x = 0.01\,\mathrm{pc}$). We find reasonable convergence for resolutions of $\gtrsim 200^3$ grid cells ($\Delta x \lesssim 0.02\,\mathrm{pc}$).

APPENDIX B: CHOICE OF DENSITY THRESHOLD

In this study, we use a threshold for the number density, $n_{\mathrm{threshold}} = 10^2\,\mathrm{cm}^{-3}$, for selecting dense, cold gas, representing the minimum number density where the transition from atomic to molecular gas via surface reactions on dust grains occurs. This value is expected to be in the range 100–$1000\,\mathrm{cm}^{-3}$ as shown in, e.g. Glover & Mac Low (2007), and thus we adopt a fiducial value of $n_{\mathrm{threshold}} = 10^2\,\mathrm{cm}^{-3}$ for our main analyses. However, here we show that our results do not

significantly depend on the exact choice of $n_{\mathrm{threshold}}$, by comparing results for $n_{\mathrm{threshold}} = 10^2\,\mathrm{cm}^{-3}$–$10^3\,\mathrm{cm}^{-3}$ in Fig. B1. Apart from the initial transient phase (where the amount of gas satisfying the condition $n > 1000\,\mathrm{cm}^{-3}$ is very low and hence the error bars are very high), the values of b for both density thresholds agree to within < 10 per cent deviation. The time-averaged values of b in the driving phase are 0.76 ± 0.08 and 0.81 ± 0.12 for $n_{\mathrm{threshold}} = 10^2\,\mathrm{cm}^{-3}$ and $10^3\,\mathrm{cm}^{-3}$, respectively. We can thus conclude that adopting any value for $n_{\mathrm{threshold}}$ in the realistic range of the transition number density (100–$1000\,\mathrm{cm}^{-3}$) gives robust results.
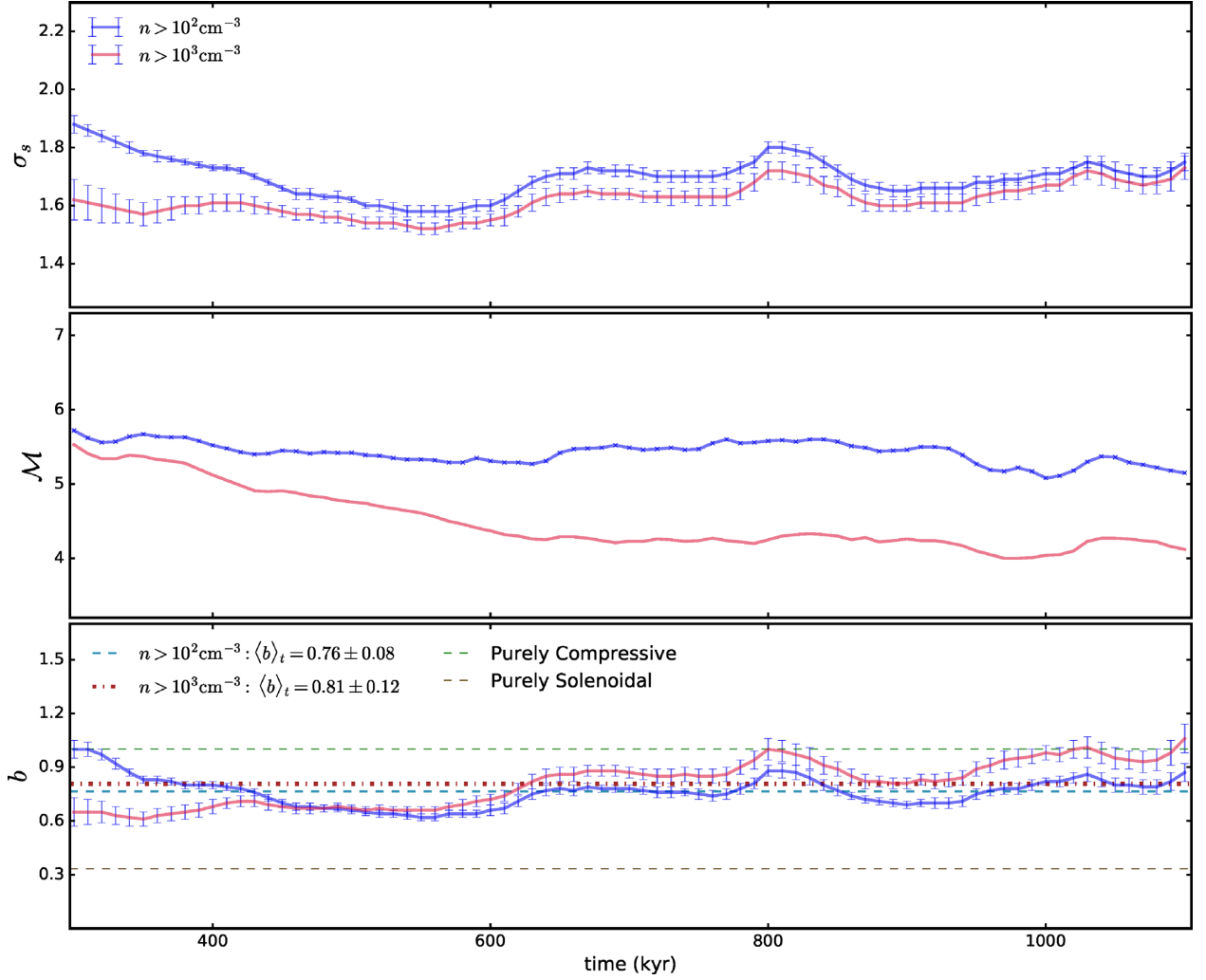
Figure B1. Comparison of derived values of σ_s, $\mathcal{M}$, and b with $n_{\text{threshold}} = 100 \, \text{cm}^{-3}$ and $1000 \, \text{cm}^{-3}$. We find that our results are not particularly sensitive to the choice of $n_{\text{threshold}}$ as long as $n_{\text{threshold}}$ is in the reasonable range 10^2–$10^3 \, \text{cm}^{-3}$ to define dense, cold gas.

APPENDIX C: VIRIAL PARAMETER METHOD

In Section 3.5, we compute the virial parameter (α_{vir}) for the pillars by calculating the ratio of their kinetic and potential energies, which are individually estimated as the sum of the local contributions to the energies by computational cells belonging to the region of interest. However, there are alternative methods used to calculate α_{vir}, and the values obtained may depend on the method. To test the dependence of α_{vir} on the method, we explore two alternative methods to calculate the virial parameter, namely

(i) using a fixed velocity dispersion. In this, case we do not take into account the individual contributions of cells in the calculation of the kinetic energies, but rather estimate it from the velocity dispersion (σ_v) for the entire pillar region. α_{vir} is then

$$\alpha_{\text{vir}} = \frac{\sigma_v^2 \sum_{i \in P} m_i}{\sum_{i \in P} m_i |\Phi_i|}, \tag{C1}$$

(ii) using an approximation that treats the pillar as if it were an isolated, spherical region. For this method, we assume the pillars can be approximated as spherical clouds of mass $M_c = \sum_{i \in P} m_i$ and

radius R_c occupying a volume $V = 4/3 \pi R_c^3 = \sum_{i \in P} V_i$, where V_i is the volume occupied by computational cell i. α_{vir} is then estimated as

$$\alpha_{\text{vir}} = \frac{5 \sigma_v^2 L}{6 G M_c}, \tag{C2}$$

where $L = 2R_c$, G is the gravitational constant, and σ_v is the velocity dispersion in the pillar. This is the method widely used in observational studies to determine α_{vir} because the 3D gravitational potential is not available in observations.

In Fig. C1, we compare the values of α_{vir} obtained with the above methods and the method used in Section 3.5. We find that α_{vir} decreases with time for the pillars in all three methods, which suggests that our basic conclusions regarding the time evolution of the pillars is independent of the choice of method. However, we note that the values of α_{vir} vary significantly with the method adopted, especially in the isolated, spherical-cloud method. This is because the definition of α_{vir} in this method is based on global parameters, assuming a spherical, homogeneous cloud. This is far from realistic, as the pillars are highly non-homogeneous and non-spherical. The
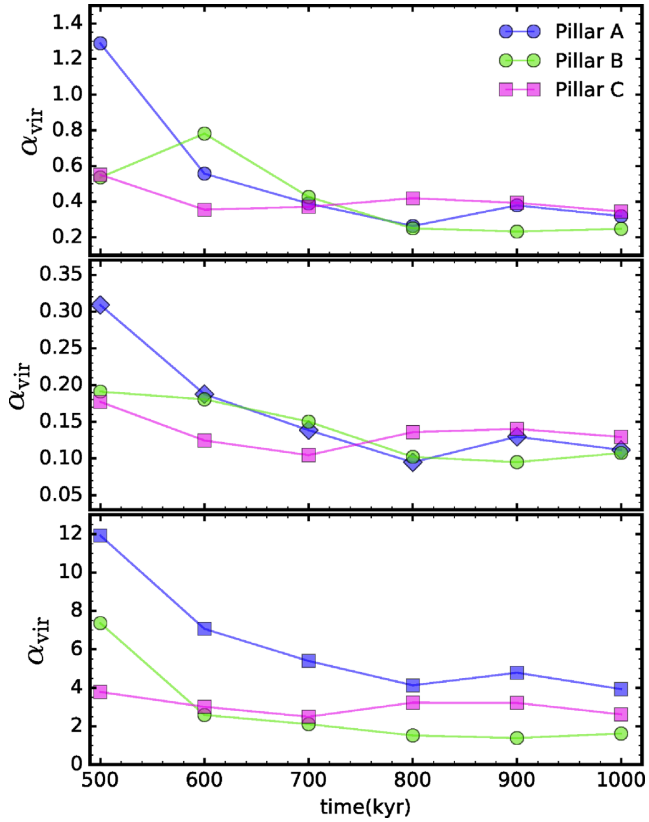
Figure C1. Evolution of the virial parameter α_{vir} with time obtained for the pillar regions using three different methods: (1) the method defined in Section 3.5, which uses all local information to compute α_{vir} (top panel), (2) using a fixed velocity dispersion (middle panel), given by equation (C1), and (3) using the isolated, spherical-cloud approximation (bottom panel), given by equation (C2). We find that our result of a decreasing trend for α_{vir} with time is robust, however, the value of α_{vir} changes significantly with the choice of method.

gas in the pillars is turbulent, and hence can be concentrated locally in fractal structures that cause a decrease in α_{vir} without necessarily increasing the total mass in the region. In addition, the spherical cloud is assumed to be isolated, and hence the dynamical effects on the gravitational potential due to the gas outside the boundary of the pillar is not considered (Federrath & Klessen 2012). The large difference in the value of α_{vir} obtained with this approximation suggests that it should be used and interpreted with caution, and may not necessarily represent the true dynamical state of the gas in the cloud.

This paper has been typeset from a TeX/LaTeX file prepared by the author.